Luminescent Charge-Transfer Platinum(II) Metallacycle

**Fei Hua,[†] Solen Kinayyigit,[†] Aaron A. Rachford,[†] Elena A. Shikhova,[†] Sébastien Goeb,[†]
John R. Cable,[†] Christopher J. Adams,[‡] Kristin Kirschbaum,[§] A. Alan Pinkerton,[§] and
Felix N. Castellano*,[†]**

*Department of Chemistry and Center for Photochemical Sciences, Bowling Green State University,
Bowling Green, Ohio 43403 School of Chemistry, University of Bristol, Bristol BS8 1TS, U.K.
Department of Chemistry, University of Toledo, Toledo, Ohio 43606*

The photophysical and electrochemical properties of a platinum(II) diimine complex bearing the bidentate diacetylide ligand tolan-2,2′-diacetylide (tda), Pt(dbbpy)(tda) [dbbpy = 4,4′-di-*tert*-butyl-2,2′-bipyridine] (**1**), are compared with two reference compounds, Pt(dbbpy)(C≡CPh)₂ (**2**) and Pt(dppp)tda [dppp = 1,3-*bis*(diphenylphosphino)propane] (**3**), respectively. The X-ray crystal structure of **1** is reported, which illustrates the nearly perfect square planarity exhibited by this metallacycle. Chromophore **2** possesses low-lying charge-transfer excited states analogous to **1**, whereas structure **3** lacks such excited states but features a low-lying platinum-perturbed tda intraligand triplet manifold. In CH₂Cl₂, **1** exhibits a broad emission centered at 562 nm at ambient temperature, similar to **2**, but with a higher photoluminescence quantum yield and longer excited-state lifetime. In both instances, the photoluminescence is consistent with triplet-charge-transfer excited-state parentage. The rigidity imposed by the cyclic diacetylide ligand in **1** leads to a reduction in nonradiative decay, which enhances its room-temperature photophysical properties. By comparison, **3** radiates highly structured tda-localized triplet-state phosphorescence at room temperature. The 77 K emission spectrum of **1** in 4:1 EtOH/MeOH becomes structured and is quantitatively similar to that measured for **3** under the same conditions. Because the 77 K spectra are nearly identical, the emissions are assigned as ³tda in nature, implying that the charge-transfer states are raised in energy, relative to the ³tda levels in **1** in the low-temperature glass. Nanosecond transient absorption spectrometry and ultrafast difference spectra were determined for **1**–**3** in CH₂Cl₂ and DMF at ambient temperature. In **1** and **2**, the major absorption transients are consistent with the one-electron reduced complexes, corroborated by reductive spectroelectrochemical measurements performed at room temperature. As **3** does not possess any charge-transfer character, excitation into the ππ* transitions of the tda ligand generated transient absorptions in the relaxed excited state assigned to the ligand-localized triplet state. In all three cases, the excited-state lifetimes measured by transient absorption are similar to those measured by time-resolved photoluminescence, suggesting that the same excited states giving rise to the photoluminescence are responsible for the absorption transients. ESR spectroscopy of the anions **1**⁻ and **2**⁻ and reductive spectroelectrochemistry of **1** and **2** revealed a LUMO based largely on the π* orbital of the dbbpy ligand. Time-dependent density functional theory calculations performed on **1**–**3** both in vacuum and in a CH₂Cl₂ continuum revealed the molecular orbitals, energies, dipole moments, and oscillator strengths for the various electronic transitions in these molecules. A ΔSCF-method-derived shift applied to the calculated transition energies in the solvent continuum yielded good agreement between theory and experiment for each molecule in this study.

Introduction

Since the original description of Pt(phen)(C≡CPh)₂ by Che and co-workers in 1994,[1] the number of related square-planar platinum(II) acetylides bearing a lone polyimine ligand has exploded.[2–27] Such molecules have demonstrated promise in diverse applications including optical power limiting,[14,15] electroluminescence,[12] singlet-oxygen photosensitization,[16,17] photocatalytic hydrogen production,[18–20] cation sensors,[21–23] vapochromism,[24] medicinal chemistry,[25] and as extrinsic luminescent probes.[26] In general, these chromophores are rich

* To whom correspondence should be addressed. E-mail: castell@bgsu.edu.
† Bowling Green State University.
‡ University of Bristol.
§ University of Toledo.

in terms of their photophysics, combining properties of traditional coordination compounds and organometallics within the same structure. This amalgamation has inspired creativity in molecular design, uncovering new and sometimes unexpected photophysical properties in apparently straightforward platinum(II) complexes.[27] The excited-state properties of these compounds emanate from charge-transfer processes between the metal center and diimine ligand that are strongly influenced by the electronic nature of the acetylide ligands.

Platinum(II)-containing conjugated metallacycles are also emerging as a new class of structurally and electronically appealing metal-organic materials.[28−34] Although numerous metallacyclynes have been produced by a variety of research groups, their photophysical properties remain largely unexplored, despite the fact that these structural motifs should give rise to interesting excited-state behavior. In the hope of coupling metallacycle electronic structures to charge-transfer processes in platinum acetylides, we recently designed the molecule Pt(dbbpy)(tda) [dbbpy = 4,4′-di-*tert*-butyl-2,2′-bipyridine; tda = tolan-2,2′-diacetylide] (**1**).[11] In this chromophore, the diacetylide ligand is restricted to the same plane as the diimine ligand, a geometry that helps reduce nonradiative decay and improves electron delocalization in the diacetylide moiety. The significant metallacycle participation in the ground and excited states of these complexes yields a molecule with stronger and red-shifted visible absorption, higher quantum yield, and a longer excited-state lifetime than the structurally related benchmark compound Pt(dbbpy)(C≡CPh)$_2$, **2**. The original preliminary report described many aspects of the photoluminescence and electronic structures of **1** and **2**, whereas the current work provides a complete spectroscopic study and theoretical treatment of the ground- and excited-state properties of **1** and **2** along with the additional model compound Pt(dppp)-tda [dppp = 1,3-bis(diphenylphosphino)propane] (**3**). Whereas **3** contains the metal-perturbed tda ligand, it does not possess any low-energy charge-transfer character; such a chomophore is necessary for a complete understanding of tda-based $^3\pi\pi^*$ intraligand (^{3}IL) excited states that may be present in **1**.

1　　　**2**

3
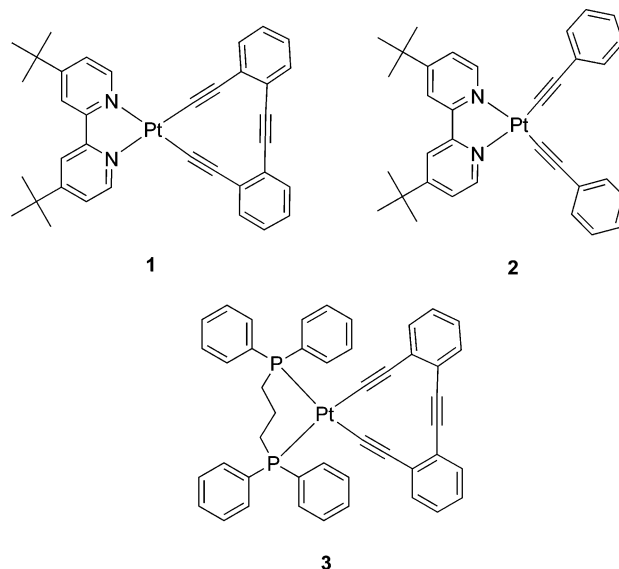
Experimental Section

General. All of the reactions were carried out under an inert and dry argon atmosphere using standard techniques. Anhydrous CH$_2$Cl$_2$, diisopropylamine, and triethylamine were freshly distilled over CaH$_2$. All of the other reagents from commercial sources were

(1) Chan, C.-W.; Cheng, L.-K.; Che, C.-M. *Coord. Chem. Rev.* **1994**, *132*, 87−97.
(2) James, S. L.; Younus, M.; Raithby, P. R.; Lewis, J. *J. Organomet. Chem.* **1997**, *543*, 233−235.
(3) Hissler, M.; Connick, W. B.; Geiger, D. K.; McGarrah, J. E.; Lipa, D.; Lachicotte, R. J.; Eisenberg, R. *Inorg. Chem.* **2000**, *39*, 447−457.
(4) Whittle, C. E.; Weinstein, J. A.; George, M. W.; Schanze, K. S. *Inorg. Chem.* **2001**, *40*, 4053−4062.
(5) McGarrah, J. E.; Eisenberg, R. *Inorg. Chem.* **2003**, *42*, 4355−4365.
(6) Adams, C. J.; James, S. L.; Liu, X.-M.; Raithby, P. R.; Yellowlees, L. J. *J. Chem. Soc., Dalton Trans.* **2000**, 63−67.
(7) Pomestchenko, I. E.; Castellano, F. N. *J. Phys. Chem. A* **2004**, *108*, 3485−3492.
(8) Hua, F.; Kinayyigit, S.; Cable, J. R.; Castellano, F. N. *Inorg. Chem.* **2005**, *44*, 471−473.
(9) Pomestchenko, I. E.; Luman, C. R.; Hissler, M.; Ziessel, R.; Castellano, F. N. *Inorg. Chem.* **2003**, *42*, 1394−1396.
(10) Danilov, E. O.; Pomestchenko, I. E.; Kinayyigit, S.; Gentilli, P. L.; Hissler, M.; Ziessel, R.; Castellano, F. N. *J. Phys. Chem. A* **2005**, *109*, 2465−2471.
(11) Hua, F.; Kinayyigit, S.; Cable, J. R.; Castellano, F. N. *Inorg. Chem.* **2006**, *45*, 4304−4306.
(12) Chan, S.-C.; Chan, M. C. W.; Wang, Y.; Che, C.-M.; Cheung, K.-K.; Zhu, N. *Chem.−Eur. J.* **2001**, *7*, 4180−4190.
(13) Adams, C. J.; Fey, N.; Weinstein, J. A. *Inorg. Chem.* **2006**, *45*, 6105−6107.
(14) Sun, W.; Wu, Z.-X.; Yang, Q.-Z.; Wu, L.-Z.; Tung, C.-H. *Appl. Phys. Lett.* **2003**, *82*, 850−852.
(15) Guo, F.; Sun, W.; Liu, Y.; Schanze, K. *Inorg. Chem.* **2005**, *44*, 4055−4065.
(16) Zhang, D.; Wu, L.-Z.; Yang, Q.-Z.; Li, X.-H.; Zhang, L.-P.; Tung, C.-H. *Org. Lett.* **2003**, *5*, 3221−3224.
(17) Yang, Y.; Zhang, D.; Wu, L.-Z.; Chen, B.; Zhang, L.-P.; Tung, C.-H. *J. Org. Chem.* **2004**, *69*, 4788−4791.
(18) Zhang, D.; Wu, L.-Z.; Zhou, L.; Han, X.; Yang, Q.-Z.; Zhang, L.-P.; Tung, C.-H. *J. Am. Chem. Soc.* **2004**, *126*, 3440−3441.
(19) Du, P.; Schneider, J.; Jarosz, P.; Eisenberg, R. *J. Am. Chem. Soc.* **2006**, *128*, 7726−7727.
(20) Narayana-Prabhu, R.; Schmehl, R. H. *Inorg. Chem.* **2006**, *45*, 4319−4321.
(21) Yang, Q.-Z.; Wu, L.-Z.; Zhang, H.; Chen, B.; Wu, Z.-X.; Zhang, L.-P.; Tung, C.-H. *Inorg. Chem.* **2004**, *43*, 5195−5197.
(22) Yang, Q.-Z.; Tong, Q.-X.; Wu, L.-Z.; Wu, Z.-X.; Zhang, L.-P.; Tung, C.-H. *Eur. J. Inorg. Chem.* **2004**, 1948−1954.
(23) Yam, V. W.-W.; Tang, R. P.-L.; Wong, K. M.-C.; Cheung, K.-K. *Organometallics* **2001**, *20*, 4476−4482.
(24) Lu, W.; Chan, M, C. W.; Zhu, N.; Che, C.-M.; He, Z.; Wong, K.-Y. *Chem.−Eur. J.* **2003**, *9*, 6155−6166.
(25) Ma, D.-L.; Shum, T. Y.-T.; Zhang, F.; Che, C.-M.; Yang, M. *Chem. Commun.* **2005**, 4765−4677.
(26) Wong, K. M.-C.; Tang, W.-S.; Chu, B. W.-K.; Zhu, N.; Yam, V. W.-W. *Organometallics* **2004**, *23*, 3459−3465.
(27) (a) Castellano, F. N.; Pomestchenko, I. E.; Shikhova, E.; Hua, F.; Muro, M. L.; Rajapakse, N. *Coord. Chem. Rev.* **2006**, *250*, 1819−1828. (b) Shikhova, E.; Danilov, E. O.; Kinayyigit, S.; Pomestchenko, I. E.; Tregubov, A. D.; Camerel, F.; Retailleau, P.; Ziessel, R.; Castellano, F. N. *Inorg. Chem.* **2007**, *46*, 3038−3048.
(28) Bradshaw, J. D.; Guo, L.; Tessier, C. A.; Youngs, W. J. *Organometallics* **1996**, *15*, 2582−2584.
(29) Guo, L.; Bradshaw, J. D.; McConville, D. B.; Tessier, C. A.; Youngs, W. J. *Organometallics* **1997**, *16*, 1685−1692.
(30) Youngs, W. J.; Tessier, C. A.; Bradshaw, J. D. *Chem. Rev.* **1999**, *99*, 3153−3180.
(31) Pak, J. J.; Weakley, T. J. R.; Haley, M. M. *Organometallics* **1997**, *16*, 4505−4507.
(32) Johnson, C. A.; Haley, M. M.; Rather, W.; Han, F.; Weakley, T. J. R. *Organometallics* **2005**, *24*, 1161−1172.
(33) Bosch, E.; Barnes, C. L. *Organometallics* **2000**, *19*, 5522−5524.
(34) Campbell, K.; McDonald, R.; Ferguson, M. J.; Tykwinski, R. R. *Organometallics* **2003**, *22*, 1353−1355.

used as received. ^{1}H NMR and ^{13}C-{^{1}H} NMR spectra were recorded on a Bruker Avance 300 (300 MHz) spectrometer. ^{31}P NMR spectra were recorded on a Varian Unity 400 (400 MHz). In the case of ^{31}P{^{1}H} NMR, chemical shifts are reported relative to 85% H_3PO_4, used as an external standard. All of the other chemical shifts are referenced to the residual solvent signals previously referenced to TMS, and splitting patterns are designated as s (singlet), d (doublet), t (triplet), q (quartet), m (multiplet), and br (broad). EI mass spectra (70 eV) were measured in-house using a direct-insertion probe in a Shimadzu QP5050A spectrometer. FTIR spectra were measured by a ThermoNicolet IR 200 spectrometer equipped with an ATR accessory. Elemental analyses were performed by Atlantic Microlab, Norcross, GA.

Preparations. Di-*o*-bromotolane,[35] bis-*o*-{(trimethylsilyl)ethynyl}-tolane,[29] di-*o*-ethynyltolane {(OBET)H$_2$},[29] Pt(dbbpy)Cl$_2$,[36] Pt-(dppp)Cl$_2$,[37] and Pt(dbbpy)(C≡C−Ph)$_2$ (**2**)[2−4] were synthesized according to literature procedures and yielded satisfactory mass and ^{1}H NMR spectra.

Pt(dbbpy)(tda) (1).[11] Pt(dbbpy)Cl$_2$ (0.53 g, 1 mmol) and CuI (1.9 mg, 0.1 mmol) were placed in a sealable reaction vessel. A solution of CH_2Cl_2 and diisopropylamine (5:1) (180 mL) was degassed for 15 min and added to the flask. (OBET)H$_2$ (0.23 g, 1 mmol) was then added to the reaction mixture, which was sealed with a Teflon screw-cap fitted with an o-ring and stirred at room temperature for 3 days. The solvent was removed under vacuum, and the residue was obtained as a dark-orange powder. The powder was dissolved in CH_2Cl_2, washed with H_2O, and the organic fractions were dried over $MgSO_4$. Evaporation of the CH_2Cl_2 gave a brown powder. Purification by chromatography on alumina eluting with a mixture of 4:1 CH_2Cl_2/CH_3CN gave the pure-yellow powder (0.62 g, 90%). ^{1}H NMR (CD$_2$Cl$_2$): δ 9.66 (m, 2H), 8.06 (d, 2H), 7.66 (m, 4H), 7.58 (m, 2H), 7.33 (m, 2H), 7.24 (m, 2H), 1.51 (s, 18H). ^{13}C-{^{1}H}NMR (CD$_2$Cl$_2$): δ 163.9, 156.3, 151.7 (pyridyl), 131.6, 130.8, 129.9, 127.4, 127.3, 125.0 (tda), 124.9 (pyridyl), 119.2 (pyridyl), 100.8, 93.2 (Pt−*C*≡C−), 92.9 (Pt−C≡*C*−), 35.8, 30.0. EI-MS (70 eV): *m/z* 687. Anal. Calcd for C$_{36}$H$_{32}$N$_2$Pt·CH$_2$Cl$_2$: C, 57.51; H, 4.44; N, 3.63. Found: C, 57.57; H, 4.44; N, 3.62. FTIR (ATR): 2111 cm^{-1} ($\nu_{C≡C}$).

Pt(dppp)(tda) (3). The same procedure for **1** was utilized except Pt(dppp)Cl$_2$ (0.27 g, 0.4 mmol) was used as the starting material, and the other reagents were present in the same ratio as above. Purification by chromatography on alumina, eluting with a mixture of 4:1 CH_2Cl_2/CH_3CN yielded a yellow powder (0.15 g, 45%). ^{1}H NMR (CD$_2$Cl$_2$): δ 7.83 (m, 8H), 7.57 (m, 2H), 7.45 (m, 12H), 7.12 (m, 4H), 6.79 (m, 2H), 2.64 (m, 4H), 2.02 (m, 2H). ^{31}P-{^{1}H}-NMR (126 MHz, CDCl$_3$): δ −6.08 ($J_{Pt−P}$ = 2222 Hz). EI-MS (70 eV): *m/z* 832. Anal. Calcd for C$_{45}$H$_{34}$P$_2$Pt·H$_2$O: C, 63.60; H, 4.27. Found: C, 63.67; H, 4.07. FTIR (ATR): 2117 cm^{-1} ($\nu_{C≡C}$).

Photophysical Measurements. Static UV−vis absorption spectra were measured with a Hewlett-Packard 8453 diode array spectro-photometer, accurate to ± 2 nm. Steady-state photoluminescence spectra were obtained with a single photon counting spectrofluo-rimeter from Edinburgh Analytical Instruments (FL/FS 900) or a QM-4/2006SE from Photon Technologies Inc. Solutions prepared for all of the photophysical experiments were optically dilute for steady-state photoluminescence (OD = 0.09−0.11) and for emission lifetime determination (OD = 0.01), whereas nanosecond transient absorption experiments utilized higher concentrations (OD = ∼0.2−

0.8). In most instances, luminescence and nanosecond transient absorption samples in 1 cm path length anaerobic quartz cells (Starna Cells) were deoxygenated with solvent-saturated argon for at least 20 min prior to measurement. Ultrafast transient absorption measurements utilized 2 mm path length optical cells. Photolumi-nescence quantum yields were separately verified in a specially designed optical cell bearing a sidearm round-bottom flask, where samples were subjected to a minimum of three freeze−pump−thaw cycles. Data from simple deaeration with argon gas and freeze−pump−thaw cycles quantitatively yielded the same results. Photoluminescence quantum yields were determined relative to [Ru-(bpy)$_3$]$^{2+}$ in deaerated acetonitrile (Φ_{em} = 0.062).[38,62] Emission lifetimes were measured using a nitrogen-pumped broadband dye laser (PTI GL-3300 N2 laser, PTI GL-301 dye laser, C-460 dye for **1** and **2**; BPBD for **3**) as the excitation source.[38] Pulse energies were typically attenuated to ∼ 50 μJ/pulse, measured with a Molectron Joulemeter (J4−05). An average of 64 transients

(38) Tyson, D. S.; Castellano, F. N. *J. Phys. Chem. A* **1999**, *103*, 10955−10960.
(39) Tyson, D. S.; Henbest, K. B.; Bialecki, J.; Castellano, F. N. *J. Phys. Chem. A* **2001**, *105*, 8154−8161.
(40) DeAngelis, T. P.; Heineman, W. R. *J. Chem. Educ.* **1976**, *53*, 594−597.
(41) Frisch, M. J.; Trucks, G. W.; Schlegel, H. B.; Scuseria, G. E.; Robb, M. A.; Cheeseman, J. R.; Montgomery, J. A., Jr.; Vreven, T.; Kudin, K. N.; Burant, J. C.; Millam, J. M.; Iyengar, S. S.; Tomasi, J.; Barone, V.; Mennucci, B.; Cossi, M.; Scalmani, G.; Rega, N.; Petersson, G. A.; Nakatsuji, H.; Hada, M.; Ehara, M.; Toyota, K.; Fukuda, R.; Hasegawa, J.; Ishida, M.; Nakajima, T.; Honda, Y.; Kitao, O.; Nakai, H.; Klene, M.; Li, X.; Knox, J. E.; Hratchian, H. P.; Cross, J. B.; Bakken, V.; Adamo, C.; Jaramillo, J.; Gomperts, R.; Stratmann, R. E.; Yazyev, O.; Austin, A. J.; Cammi, R.; Pomelli, C.; Ochterski, J. W.; Ayala, P. Y.; Morokuma, K.; Voth, G. A.; Salvador, P.; Dannenberg, J. J.; Zakrzewski, V. G.; Dapprich, S.; Daniels, A. D.; Strain, M. C.; Farkas, O.; Malick, D. K.; Rabuck, A. D.; Raghavachari, K.; Foresman, J. B.; Ortiz, J. V.; Cui, Q.; Baboul, A. G.; Clifford, S.; Cioslowski, J.; Stefanov, B. B.; Liu, G.; Liashenko, A.; Piskorz, P.; Komaromi, I.; Martin, R. L.; Fox, D. J.; Keith, T.; Al-Laham, M. A.; Peng, C. Y.; Nanayakkara, A.; Challacombe, M.; Gill, P. M. W.; Johnson, B.; Chen, W.; Wong, M. W.; Gonzalez, C.; Pople, J. A. *Gaussian 03*, revision B.05; Gaussian, Inc.: Wallingford, CT, 2004.
(42) Becke, A. D. *J. Chem. Phys.* **1993**, *98*, 5648−5652.
(43) Lee, C.; Yang, W.; Parr, R. G. *Phys. Rev. B* **1988**, *37*, 785−789.
(44) Hay, P. J.; Wadt, W. R. *J. Chem. Phys.* **1985**, *82*, 299−310.
(45) Miertus, S.; Scrocco, E.; Tomasi, J. *Chem. Phys.* **1981**, *55*, 117−129.
(46) Rappé, A. K.; Casewit, C. J.; Colwell, K. S.; Goddard, W. A, III; Skiff, W. M. *J. Am. Chem. Soc.* **1992**, *114*, 10024−10035.
(47) The solute cavity was generated without the use of symmetry even though the complex structures were symmetric.
(48) *SMART*, version 5.630; Bruker AXS Inc.: Madison, WI, 2003.
(49) Sheldrick, G. M., *SADABS*; Universität Göttingen: Göttingen, Germany, 1999.
(50) Sheldrick, G. M., *SHELXTL*, version 6.14; Bruker AXS Inc.: Madison, WI, 1998.
(51) Crosby, G. A. *Acc. Chem. Res.* **1975**, *8*, 231−238.
(52) Collison, D.; Mabbs, F. E.; McInnes, E. J. L.; Taylor, K. J.; Welch, A. J.; Yellowlees, L. J. *J. Chem. Soc., Dalton Trans.* **1996**, 329−334.
(53) McInnes, E. J. L.; Farley, R. D.; Macgregor, S. A.; Taylor, K. J.; Yellowlees, L. J.; Rowlands, C. C. *J. Chem. Soc., Faraday Trans.* **1998**, *94*, 2985−2991.
(54) Connick, W. B.; Geiger, D.; Eisenberg, R. *Inorg. Chem.* **1999**, *38*, 3264−3265.
(55) Cummings, S. D.; Eisenberg, R. *J. Am. Chem. Soc.* **1996**, *118*, 1949−1960.
(56) McInnes, E. J. L.; Farley, R. D.; Rowlands, C. C.; Welch, A. J.; Rovatti, L.; Yellowlees, L. J. *J. Chem. Soc., Dalton Trans.* **1999**, 4203−4208.
(57) Casida, M. E.; Gutierrez, F.; Guan, J.; Gaeda, F.-X.; Salahub, D.; Daudey, J.-P. *J. Chem. Phys.* **2000**, *113*, 7062−7071.
(58) Dreuw, A.; Weisman, J. L.; Head-Gordon, M. *J. Chem. Phys.* **2003**, *119*, 2943−2946.
(59) Tozer, D. *J. Chem. Phys.* **2003**, *119*, 12697−12699.
(60) Gritsenko, O.; Baerends, J. *J. Chem. Phys.* **2004**, *1121*, 655−660.
(61) Dreuw, A.; Head-Gordon, M. *J. Am. Chem. Soc.* **2004**, *126*, 4007−4016.
(62) Caspar, J. V.; Meyer, T. J. *J. Am. Chem. Soc.* **1983**, *105*, 5583−5590.

(35) Waybright, S. M.; McAlpine, K.; Laskoski, M.; Smith, M. D.; Bunz, U. H. F. *J. Am. Chem. Soc.* **2002**, *124*, 8661−8666.
(36) Hodges, K. D.; Rund, J. V. *Inorg. Chem.* **1975**, *14*, 525−528.
(37) Appleton, T. G.; Bennett, M. A.; Tompkins, B. *J. Chem. Soc., Dalton Trans.* **1976**, 439−446.

was collected, transferred to a computer, and processed using Origin 7.5. Frozen glass emission samples at 77 K in 4:1 EtOH/MeOH were prepared by inserting a 5 mm inner diameter NMR tube containing the relevant solution (OD = 0.05 for **1** and **2**; OD = 0.5 for **3**) into a quartz-tipped finger dewar containing liquid nitrogen. Nanosecond transient absorption spectrometry was performed using the same probe and detection apparatus previously described;[39] however, a different pump laser system was employed (Spectra Physics Quanta Ray PRO 230 Nd:YAG laser equipped with a MOPO SL optical parametric oscillator). The attenuated third harmonic output of the YAG laser (355 nm) was used to pump the samples; alternatively, the full-power 355 nm YAG output pumped the MOPO system to produce the desired 430 nm visible output. In this experiment, the probe lamp is not pulsed so that intense emission artifacts, like those from the high-quantum-yield emitters **1** and **2**, cannot be properly removed or corrected for in this apparatus. Therefore, no information is available on long-wavelength absorption transients acquired on the nanosecond/microsecond time scale. For completeness, long-wavelength transients measured in ultrafast experiments are provided as Supporting Information; the complete ultrafast transient absorption study on **1**−**3** is in progress and will be published elsewhere in the near future. These ultrafast measurements were performed on the same apparatus as previously published.[10] Time-resolved emission spectra were acquired using a computer-controlled Nd:YAG laser/OPO system from OPOTEK (Vibrant-LD) tuned at the low-energy absorption maximum for each compound. A Micro HR Horiba/JY spectrograph equipped with a 300 gr/mm grating interfaced with an Andor iSTAR iCCD served as the detection system.

Electrochemistry. Electrochemical measurements were performed in DMF (anhydrous, Acros) using 0.1 M [*n*-Bu₄N][ClO₄] (TBAP) as a supporting electrolyte at room temperature. This solvent was purposely selected because it provides superior stability in ambient reductive spectroelectrochemical experiments. We note that in the previous communication, the first oxidation and first reduction potentials of **1** and **2** are reported in CH_2Cl_2/0.15 M TBAP.[11] A three-electrode arrangement was utilized, where a platinum disk working electrode (BAS model MF-2013), a platinum wire auxiliary electrode (CH Instruments model CHI-115), and a Ag/AgCl (3M NaCl) reference electrode (BAS model MF-2079) were used for all of the measurements. The solutions were degassed with argon prior to each experiment, and the inert-gas purge was maintained throughout the experiments. For all of the measurements, potentials are reported relative to Ag/AgCl (3M NaCl), where $E_{1/2}([FeCp_2]^{+/0})$ = +0.55 V ($\Delta E = E_{pa} - E_{pc}$ = 81 mV) was determined in DMF. No *iR* compensation was used. The cyclic and differential pulse voltammograms were recorded with a Bioanalytical Systems Epsilon controller interfaced with a Pentium PC.

UV−Vis Absorption Spectroelectrochemistry. Spectroelectrochemical measurements were performed using an optically transparent thin layer electrode (OTTLE) cell.[40] This home-built apparatus consists of a gold-gauze working electrode, a platinum counter electrode, and a Ag/AgCl (3 M NaCl) reference electrode. The gold-gauze working electrode was prepared by bringing together quartz microscope slides (ESCO Products, Inc., Model R130110) with the gold gauze (52 mesh woven from 0.102 mm diameter wire (Alfa Aesar, Model 40930)) and sealed using Varian Torr Resin Sealant (Varian, Inc. Model 9530001). The optical cell was placed in a plexiglass box with quartz windows, which was mounted in the HP 8453 UV−vis spectrophotometer such that the light beam passes through the gold-grid working electrode. Solutions were prepared by dissolving 1 mM of metal complex in 0.1 M

TBAP/DMF. Samples were degassed with DMF-saturated argon gas prior to each experiment, and an inert-gas purge was maintained through the mounted plexiglass box during the measurements, to exclude oxygen and water vapor. The ground-state absorption spectrum of the sample contained within the cell at 0 V was used as the spectrometer blank. In this configuration, any changes associated with bulk reduction are observed as differences in absorption (ΔA). In all cases, the potentials were maintained at 100−200 mV more negative to the first reduction wave, using the BAS Epsilon system. An electrolysis time of 8−13 min at each potential step was usually found to be sufficient to attain equilibrium.

ESR Experiments. ESR spectra were recorded on a Bruker ESP300E spectrometer equipped with a Bruker variable-temperature accessory and a Hewlett-Packard 5350B microwave frequency counter. The magnetic field was calibrated against the resonance of the diphenylpicrylhydrazyl radical (g = 2.0037). Spectra were simulated using the Bruker WINEPR Simfonia program.

Density Functional Calculations. Density functional theory (DFT) calculations were carried out on **1**−**3** using the Gaussian 03 suite of programs.[41] The B3LYP functional[42,43] was employed in conjunction with an all-electron 6-31G(d) basis set for the nonmetal atoms (hydrogen, carbon, nitrogen, and phosphorus) and the LANL2DZ effective-core pseudopotential and corresponding set of basis functions[44] for platinum. The ground singlet state and lowest lying excited triplet state of each complex were treated using restricted and unrestricted formalisms, respectively. To characterize additional low-lying excited singlet and triplet states in these complexes, time-dependent DFT (TDDFT) calculations were carried out. Initial calculations were performed in the absence of solvent. Then, to simulate the effect of solvation by CH_2Cl_2 (ϵ = 8.93), the calculations were repeated using the polarizable continuum model[45] (PCM) as implemented in Gaussian 03. The PCM calculations were based on default integral equation formalism and employed the united atom topological model with UFF[46] atomic radii to generate the solute cavity.[47]

X-ray Crystallography. Single crystals of **1** were slowly grown from CD_2Cl_2 solution at room temperature in a NMR tube. Crystal data were collected at 120 K with a Bruker platform diffractometer (graphite-monochromated, Mo Kα = 0.071073 nm) equipped with a Smart 6000 CCD detector[48] and an Oxford Cryostream 600 low-temperature device. A crystal with the dimensions 0.58 × 0.06 × 0.05 mm was mounted on a 0.1 mm capillary with oil. Data were integrated using *SAINT 6.45A*;[48] corrections for absorption and decay were applied using *SADABS*.[49] A partial structure solution was obtained by direct methods, and remaining atoms were located with difference Fourier techniques. All of the calculations were performed using *SHELXTL 6.14*.[50] All of the unique reflections were used in the full-matrix least-squares refinement on F^2.

Results and Discussion

Preparations. All three Pt(II) complexes used in this study were prepared in accordance with standard procedures, with final purification achieved by chromatography over alumina. All of the complexes are stable solids at room temperature and are readily soluble in a variety of organic solvents. **1**−**3** were structurally characterized by NMR, mass spectrometry, elemental analysis, and FTIR. Structure **3** lacks a low-lying charge-transfer state and is used to model the ³IL manifold resident on the tda ligand, whereas **2** is intended to represent the charge-transfer triplet state in **1**.

(#1): x,-y+1/2,z
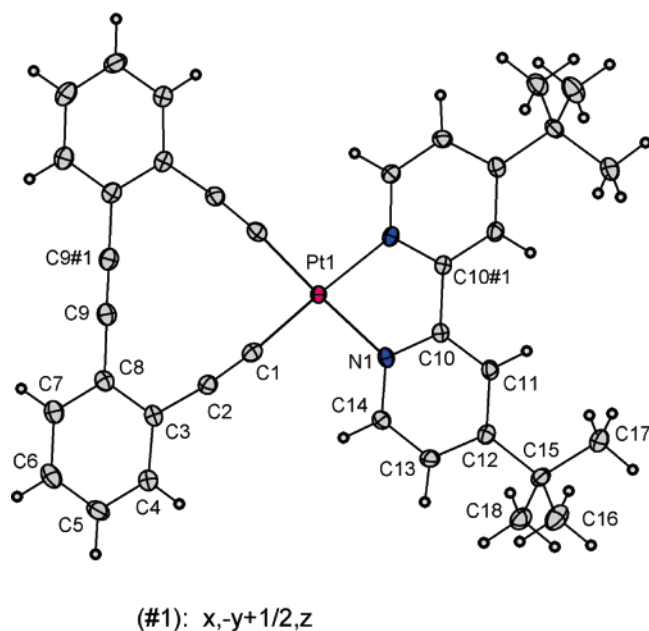
Figure 1. ORTEP drawing of **1**. Thermal ellipsoids are depicted at the 50% probability level.

Table 1. Crystal Data and Structure Refinement for **1**

empirical formula	$C_{37} H_{34} Cl_2 N_2 Pt$
fw	772.65
T, K	120(2)
wavelength	0.71073
cryst syst, space group	orthorhombic, *Pnma*
a, Å	19.1697(8)
b, Å	23.1397(10)
c, Å	7.2102(3)
V, Å^3	3198.3(2)
ρ_{calcd}, mg/m^3	1.605
μ, mm^{-1}	4.583
F(000)	1528
θ-range, deg	1.76 to 28.28
limiting indices	$-25 \leq h \leq 25, -30 \leq k \leq 30, -9 \leq l \leq 9$
reflns collected/unique	37 341/4075 [R(int) = 0.0329]
completeness to $\theta = 26.00$	100.0%
refinement method	Full-matrix least-squares on F^2
data/restraints/params	4075/0/192
GOF on F^2	1.045
final R indices [$I > 2\sigma(I)$]^a	R1 = 0.0279, wR2 = 0.0651
R indices (all data)^a	R1 = 0.0347, wR2 = 0.0689
largest diff. peak and hole	1.864 and -1.566 e.A^{-3}

^{a} R1 = $\Sigma||F_o| - |F_c||/\Sigma|F_o|$; wR2 = $\{\Sigma[w(|F_o|^2 - |F_c|^2)^2]/\Sigma[w(F_o^4)]\}^{1/2}$

Structure Description. Single crystals of **1** were obtained by slow evaporation of a CD_2Cl_2 solution. The crystal structure determined by X-ray diffraction is shown in Figure 1. The positional and thermal parameters as well as selected bond lengths and angles are collected in Tables 1 and 2. Complete tabulations of refined positional and thermal parameters and all of the bond distances and angles can be found in the CIF, which is available as Supporting Information. The coordination geometry of the Pt(II) center is essentially square planar. The Pt−N bond distance (2.059-(3) Å), N−Pt−N bond angle (79.02(14)°), and Pt−C bond distance (1.943(3) Å) agree well with other structural reports of square-planar platinum diimine complexes. The constraints of the 11-membered chelate ring lead to a C−Pt−C bond angle of 84.48(18)°, which is similar to closely related
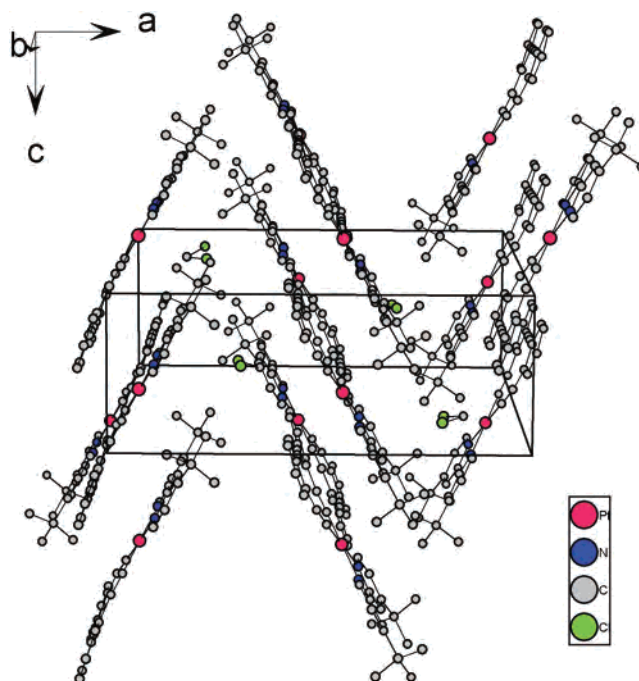
Figure 2. Solid-state packing diagram for **1**.

Table 2. Selected Bond Lengths (Angstroms) and Angles (Degrees) for **1**^{a}

Pt(1)−C(1)	1.943(3)	C(2)−C(3)	1.430(4)
Pt(1)−C(1)#1	1.943(3)	C(3)−C(4)	1.399(5)
Pt(1)−N(1)	2.059(3)	C(3)−C(8)	1.420(4)
Pt(1)−N(1)#1	2.059(3)	C(7)−C(8)	1.403(4)
N(1)−C(10)	1.358(4)	C(8)−C(9)	1.433(5)
C(1)−C(2)	1.215(4)	C(9)−C(9)#1	1.198(7)
C(1)−Pt(1)−C(1)#1	84.48(18)	C(1)−C(2)−C(3)	171.1(3)
C(1)−Pt(1)−N(1)	98.25(12)	C(4)−C(3)−C(8)	118.4(3)
C(1)#1−Pt(1)−N(1)	177.26(11)	C(8)−C(3)−C(2)	119.9(3)
C(1)−Pt(1)−N(1)#1	177.26(11)	C(7)−C(8)−C(9)	120.0(3)
N(1)−Pt(1)−N(1)#1	79.02(14)	C(3)−C(8)−C(9)	120.5(3)
C(2)−C(1)−Pt(1)	174.6(3)	C(9)#1−C(9)−C(8)	179.6(2)

^{a} Symmetry transformations used to generate equivalent atoms: (1): *x*, $-y + 1/2$, *z*.

platinum(II) metallacycles.[28] **1** has crystallographic mirror symmetry, the platinum atom lying in the plane, yielding approximate C_{2v} symmetry in the solid state.

Figure 2 gives a view down the crystallographic *b* axis, showing the packing of the molecules of **1**. The structure contains equal amounts of **1** and a dichloromethane solvent molecule, which is disordered over two positions. The refined model contained two different chlorine positions with equal occupancies for each of the chlorine atoms. Disordered hydrogen atoms were not included in the refinement. Non-hydrogen atoms were refined with anisotropic atomic displacement parameters, with the exception of the disordered chlorine atoms, which were refined with isotropic atomic displacement factors. The hydrogen atoms of the platinum complex were calculated on idealized positions and included in the refinement as riding atoms. The isotropic atomic displacement factors of the hydrogen atoms were constrained to the U_{eq} of the bonding atom.

Electrochemistry. Cyclic and differential pulse voltammograms were obtained in DMF using a Ag/AgCl (3 M NaCl) reference electrode. **1** and **2** display a reversible ($i_{pc}/$
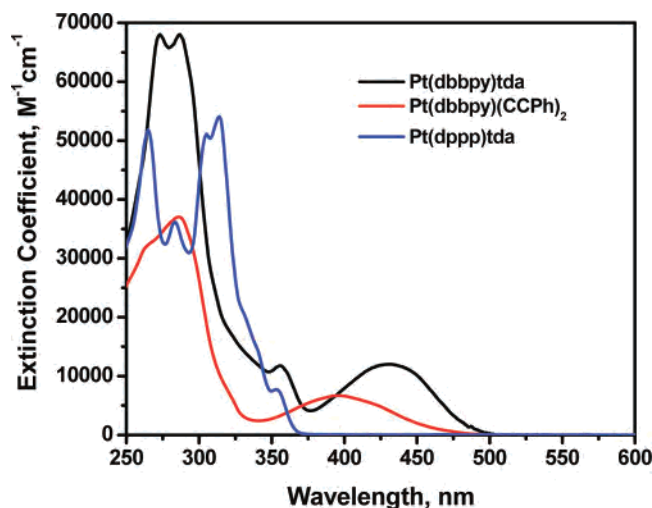
Figure 3. UV−vis absorption spectra of **1**, **2**, and **3** in CH_2Cl_2.

Figure 4. Static photoluminescence spectra of **1** (solid line), **2** (dashed line), and **3** (dotted line) in deaerated CH_2Cl_2.

Figure 5. Static photoluminescence spectra of **1** (solid line), **2** (dashed line), and **3** (dotted line) in 4:1 EtOH/MeOH glasses at 77 K.

$i_{pa}{\sim}1$) dbbpy-based reduction at −1.24 and −1.25 V versus Ag/AgCl, respectively. The oxidation processes measured for **1** and **2** in DMF were not reversible and are ill-defined. Peak anodic processes of +0.91 and +0.92 respectively (vs Fc^+/Fc^0)[11] were determined previously in CH_2Cl_2,[11] illustrating commonalities in their ground-state electronic structures. The model **3** exhibits two irreversible oxidations at +1.16 and +1.38 V versus Ag/AgCl, which are not well defined. There is also a dppp-centered reduction at −2.24 V versus Ag/AgCl, which is only observable by differential pulse voltammetry. The large differences in reduction potential between the dbbpy and dppp illustrate that low charge-transfer transitions are only likely to occur in **1** and **2** and not in **3**.

Room-Temperature Absorption and Photoluminescence. The room-temperature spectroscopic and photophysical properties of all three complexes investigated in this study are collected in Table 3. Figure 3 displays the absorption spectra of the three complexes measured in CH_2Cl_2. The low-energy absorption in **1** is red-shifted 30 nm relative to **2**, suggesting significant σ-donation of tda electron density to the Pt(II) center and is qualitatively similar in band shape. Negative solvatochromism has been previously observed for **1** and **2** and results from the large ground-state dipole moment commonly associated with these and related structures, which are in direct opposition to the excited-state dipole of a lower magnitude.[5,7,11] The higher-energy ligand-localized $\pi\pi^*$ transitions between 300 and 350 nm, resulting from electronic transitions within the acetylide fragments, are not significantly perturbed by solvent polarity.[4,5,7,12] In **3**, the low-energy tda-based $\pi\pi^*$ transitions are ligand-localized and therefore do not exhibit any significant charge-transfer character.

The photoluminescence spectra of **1**−**3**, measured in CH_2Cl_2 at room temperature, are displayed in Figure 4. The spectrum of **1** is broad, structureless, and quantitatively similar to the spectrum observed for **2**. In the case of **3**, the emission appears to be most consistent with triplet phosphorescence emanating from the tda moiety and gives a blue-shift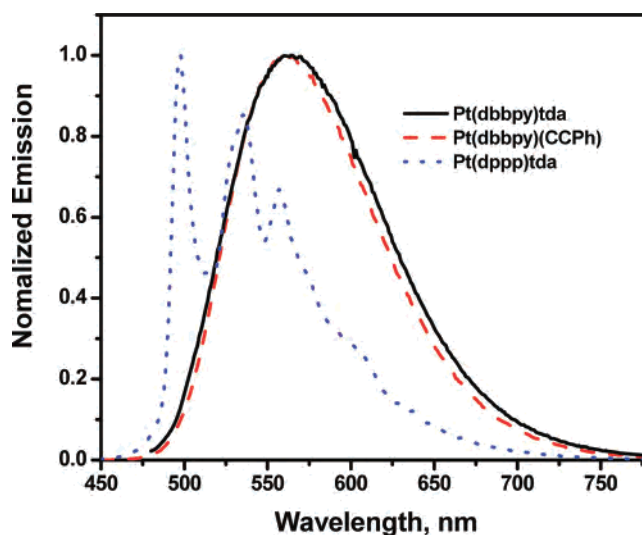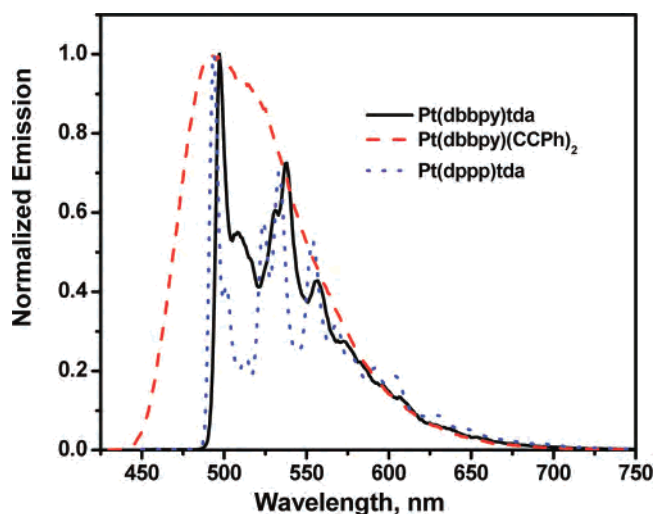ed, sharp, and structured spectrum by comparison. For the most part, the emission spectra are largely unaffected by the nature of the solvent medium. The excited-state lifetime of **1** measured by transient luminescence was determined to be 2.56 ± 0.10 μs in argon-saturated CH_2Cl_2, whereas the complementary experiment performed on **2** yields a lifetime of 1.36 ± 0.10 μs. Since the previous report,[11] we discovered a problem in one of our degassing lines, which led to underestimated quantum yield values for **1** and **2**. However, the relative differences remained essentially the same, so this did not bias any of our previous conclusions. The updated values reported here have been independently verified using freeze−pump−thaw degassing. The quantum yields of **1** and **2** measured in deaerated CH_2Cl_2 are 0.75 and 0.51, respectively, and the latter value is in quantitative agreement with that previously measured by Che and co-workers for the same compound in this solvent.[12] Impressively, **1** possesses a photoluminescence quantum yield that is extraordinarily high for a Pt(II)-based charge-transfer chromophore. When the quantum yields and excited-state lifetimes are taken into account in both molecules, the calculated values of k_r and k_{nr} (Table 3) help justify the

Table 3. Photophysical Properties of **1**–**3** in CH_2Cl_2

complex	λ_{abs}, nm	λ_{em}, nm	$\Phi_{em}{}^{a,b}$	$\tau_{em}{}^{b}$, μs	$\tau_{77K}{}^{c}$, μs	$\tau_{TA}{}^{d}$, μs	$k_r{}^{e}$ s^{-1}	$k_{nr}{}^{f}$ s^{-1}
1	427	562	0.75	2.56	9.0, 20.5 9.1, 16.5^g	2.15	2.9×10^5	9.8×10^4
2	397	560	0.51	1.36	3.51	1.22	3.8×10^5	3.6×10^5
3	355	497 536 557		13.8	70.5 72.6^g	12.1		

^{a} Argon-degassed solutions at room temperature. ^{b} PL quantum yields and intensity decays at room temperature, ±5%. ^{c} PL lifetime at 77 K determined in 4:1 EtOH:MeOH glasses. ^{d} Excited-state lifetimes determined by transient absorption at room temperature, ±10%. ^{e} $k_r = \Phi_{em}/\tau_{em}$. ^{f} $k_{nr} = (1-\Phi_{em})/\tau_{em}$. ^{g} PL lifetime at 77 K determined in MTHF glasses.

observed enhanced photoluminescence properties of **1** relative to **2**. This augmentation must result from the structural differences between the chromophores because they are practically identical from an energetic standpoint. The extended lifetime and enhanced quantum yield of **1** over **2** most likely results from the rigidity imposed by the cyclic diacetylide ligand, which leads to a measurable reduction in k_{nr}. The excited state of **3** exhibits single-exponential decay kinetics over its entire emission profile and has a lifetime of 13.8 μs in degassed CH_2Cl_2. This somewhat-extended lifetime can be considered a characteristic of tda-based ^{3}IL room-temperature phosphorescence in the presence of the internal Pt(II) heavy atom.[11] Nanosecond transient absorption spectra (below) help provide definitive assignments for the origin of the emitting states in all of these molecules.

Low-Temperature Photoluminescence. Figure 5 presents the 77 K spectra of **1**–**3** measured in 4:1 EtOH/MeOH glasses. The band shape and profile of **1** is markedly distinct from those observed in **2** but is strikingly similar to **3**. The spectrum of **2** is assigned to the charge-transfer excited state as previously observed,[3,4,7] and the complex exhibits a thermally induced Stokes shift ($\Delta E_s = E_{00}$(77 K) $- E_{00}$(298 K)) of 2450 cm^{-1}, a value commonly observed in Pt(II) diimine acetylide charge-transfer photoluminescence.[4,7] The ΔE_s values of **1** and **3** are 2300 and 120 cm^{-1}, respectively, the latter value illustrating the lack of molecular reorganization in the evolution of the tda ^{3}IL emission. Interestingly, the ΔE_s value associated with **1** is most consistent with a charge-transfer emission, but its profile completely transforms in going from room temperature to 77 K. This transformation occurs because the charge-transfer triplet-state energy at 77 K is raised above that of the ^{3}tda level, and the lower manifold dominates the observed photophysical response. The three major sharp peaks seen in the emission spectrum of **1** at 77 K occur at 20 121, 18 622, and 17 953 cm^{-1}, which are within the experimental error of those observed in **3** (20 243, 18 762, and 18 051 cm^{-1}) under identical conditions. Subtraction of the two lower-energy vibrational spacings from the origin peak yields 1499 and 2167 cm^{-1} for **1** and 1481 and 2192 cm^{-1} for **3**, respectively. The coincidence of the emission spectra in these two molecules strongly suggests that the excited states of **1** and **3** are localized on the tda ligand at 77 K. The lifetime of **2** at 77 K is 3.51 ± 0.1 μs and is well-modeled by a single-exponential function. In the case of **1**, the 77 K lifetime is complex and is most adequately modeled by the sum of two single-exponential functions in both 4:1 EtOH/MeOH ($\tau_1 = 9.0$ μs; $\tau_2 = 20.5$ μs) and MTHF ($\tau_1 = 9.1$ μs; $\tau_2 = 16.5$

μs). The intensity decay curves are largely invariant to the monitoring wavelength throughout the emission profile, and the recovered fitting parameters reveal no systematic changes in the relative amplitudes of the long and short lifetime components as a function of monitoring wavelength. Serial dilution of these samples did not change the nature of the biexponential decay curves. Detailed analyses of representative data are provided as Supporting Information and clearly demonstrate the necessity for biexponential fitting in these samples. Time-resolved emission spectra of **1** in 4:1 EtOH/MeOH (Figures S1 and S2 in the Supporting Information) reveal that there is a small spectral blue shift with time that is accompanied by band narrowing. This result suggests that there are two identifiable emitting states at 77 K, with long lifetimes and near co-incident spectral profiles. The emitting state with the broader emission profile has the shorter lifetime and is likely ^{3}CT in nature, whereas the longer-lifetime species with the structured features observed at all delay times is probably from the ^{3}IL state. In each low-temperature glass, both time constants are significantly longer than the single-exponential lifetime of **2** measured under the same conditions. The lifetime of **3** independently measured in 4:1 EtOH/MeOH and MTHF are both cleanly single exponential ($\tau = 70.5$ and 72.6 μs, respectively) and must be derived exclusively from tda-localized triplet-state phosphorescence. Time-resolved emission spectra (Figures S5–S7 in the Supporting Information) of **3** in 4:1 EtOH/MeOH at 77 K shows no variation of emission wavelength as a function of time over the entire time course of excited-state decay. Because the recovered lifetimes in **1** are complex and are extended relative to the charge-transfer **2** but are shorter than the pure ^{3}IL excited state represented by **3**; a precise assignment of the excited states in **1** at 77 K is not straightforward. What is clear is that the emission spectrum of **1** at 77 K bears strong resemblance to the model chromophore **3**, which implies that the tda ^{3}IL state lies lower in energy than the charge-transfer excited state at 77 K. This is also made apparent by comparing the low-temperature spectra of **1** and **2** in both glasses, which demonstrates that there is an inversion of triplet states taking place between room temperature and 77 K in **1**, whereas the emission from **2** is clearly charge-transfer based, at both temperature extremes. These comparative data also reveal that the energy gap between the charge-transfer and ^{3}tda states is small in **1**, producing a situation favorable for triplet-state mixing.[7,51] In this instance, one would expect the photophysics observed in **1** to represent a superposition of the charge-transfer and ^{3}tda states, yielding an intermediate excited-state lifetime,

Table 4. UV-Visible Absorption Bands of **1** and **2** before and after Controlled Potential Electrolysis (CPE) in 0.1 M TBAP/DMF

	λ, nm		
complex	oxidative CPE[a]	no. applied potential	reductive CPE[b]
1	320	275, 358, 422	315, 375, 475, 509, 600
2	323	287, 393	316, 363, 439, 480, 510, 810

[a] Corresponds to one-electron oxidative CPE at +1.50 for **1** and +1.20 V for **2**. [b] Corresponds to one-electron reductive CPE at −1.34 for **1** and −1.35 V for **2**. All of the potentials were measured relative to Ag/AgCl.

which indeed appears to be the case in **1**, albeit complex in nature. The low-temperature photophysics of **1** is dominated by the lower-energy state (^{3}tda) but is markedly influenced in its decay kinetics by the higher-lying charge-transfer state. This is quite different from the situation at room temperature where the charge-transfer state determines the photophysical outcome for this chromophore.

UV−Vis Spectroelectrochemistry. It is well-established that the first reduction of bipyridine-bearing Pt(II) complexes leads to a singly occupied molecular orbital (SOMO) that is predominately composed of the radical anion [bpy$^{•-}$].[6,52,53] Therefore, similar behavior would be anticipated for **1** and **2**, except for minor shifts in the absorption bands due to the structural differences between bpy and dbbpy. Prior to reduction, the ground-state absorption spectra of **1** and **2** are dominated by intense high-energy $\pi\pi^*$ transition bands from the dbbpy and acetylide ligands in addition to lower-energy charge-transfer bands (Figure 3 and Table 4). The shoulder at 358 nm for **1** originates from the $\pi\pi^*$ transitions of the tda ligand and should remain largely unaffected by one-electron reduction. Upon one electron reduction of **1** in 0.1 M TBAP/DMF at room temperature, the intensities of the dbbpy $\pi\pi^*$ transition bands of the below 300 nm and the charge-transfer band at 422 nm decrease, indicative of the formation of the reduced dbbpy ligand (part a of Figure 6). The new bands formed at 315, 375, 509, and 600 nm mostly correspond to intraligand electronic transitions of the dbbpy radical anion, [dbbpy$^{•-}$]. Part b of Figure 6 shows that similar spectral changes are observed upon reductive electrolysis of **2**, where new bands attributable to the formation of [dbbpy$^{•-}$] appear at 316, 363, 480, 510, and 810 nm. We note that the spectroelectrochemical data presented here for one-electron reduced **2** at room temperature is essentially identical to that measured for the same compound at 240 K.[6] After each experiment, the bias was set to 0 V, and in all instances the absorption spectrum of the starting compound was fully regenerated in both cases. With the aid of the spectroelectrochemical studies performed on **1** and **2**, we can fully assign the transient absorption spectra as described below.

Nanosecond Transient Absorption Spectroscopy. Figure 7 displays the excited-state absorption difference spectra obtained for **1** (λ_{ex} = 430 nm), **2** (λ_{ex} = 430 nm), and **3** (λ_{ex} = 355 nm) in CH$_2$Cl$_2$ recorded at several incremental delay times. In these experiments, the concentrations used were larger than in the luminescence experiments, and the excited-state lifetimes measured in the transient absorption measurements are consistently lower (Table 3). The lifetime differ-
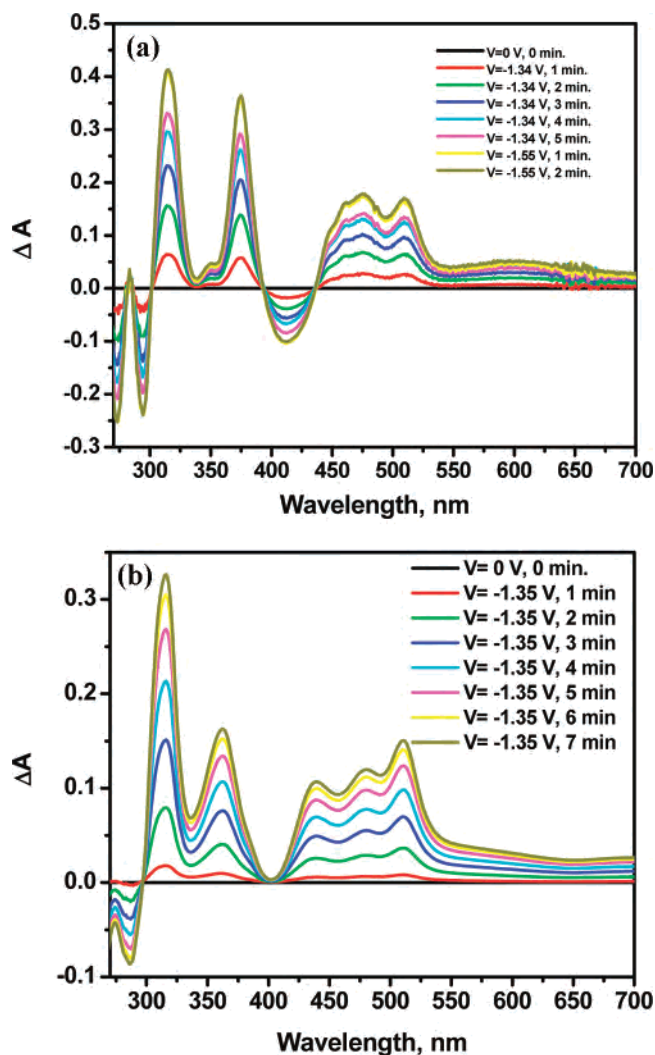
Figure 6. (a) UV−vis absorption spectral changes accompanying the reductive-controlled potential electrolysis of 1 mM of (a) **1** at $V = -1.34$ and (b) **2** at $V = -1.35$ V versus Ag/AgCl in 0.1 M TBAP/DMF.

ences observed from each technique can be accounted for by considering the well-established susceptibility of square-planar Pt(II) complexes toward self-quenching at higher concentrations.[54] This deactivation pathway results in diminished lifetimes in the transient absorption experiments relative to time-resolved photoluminescence, as we have seen in other systems previously.[7−10,27] The emitting state in each molecule is presumed to be the same as that which produces the absorption transients in all instances. Excited-state absorption difference spectra of **1−3** were obtained in CH$_2$Cl$_2$ (Figure 7) as well as DMF (Supporting Information), the latter allowing direct comparisons with spectroelectrochemistry measurements and alleviating potential concerns about the solvatochromic nature of the charge-transfer transitions. The data obtained in DMF is quantitatively similar in spectral profile and relative intensities to that observed for the same compounds in CH$_2$Cl$_2$, so the data obtained for the latter is displayed in Figure 7. The excited-state absorptions of **1** occur at ~315, ~370, and ~477 nm, with the ~315 nm band possessing slightly more intensity, part a of Figure 7. Ground-state bleaching occurs at 418 nm,
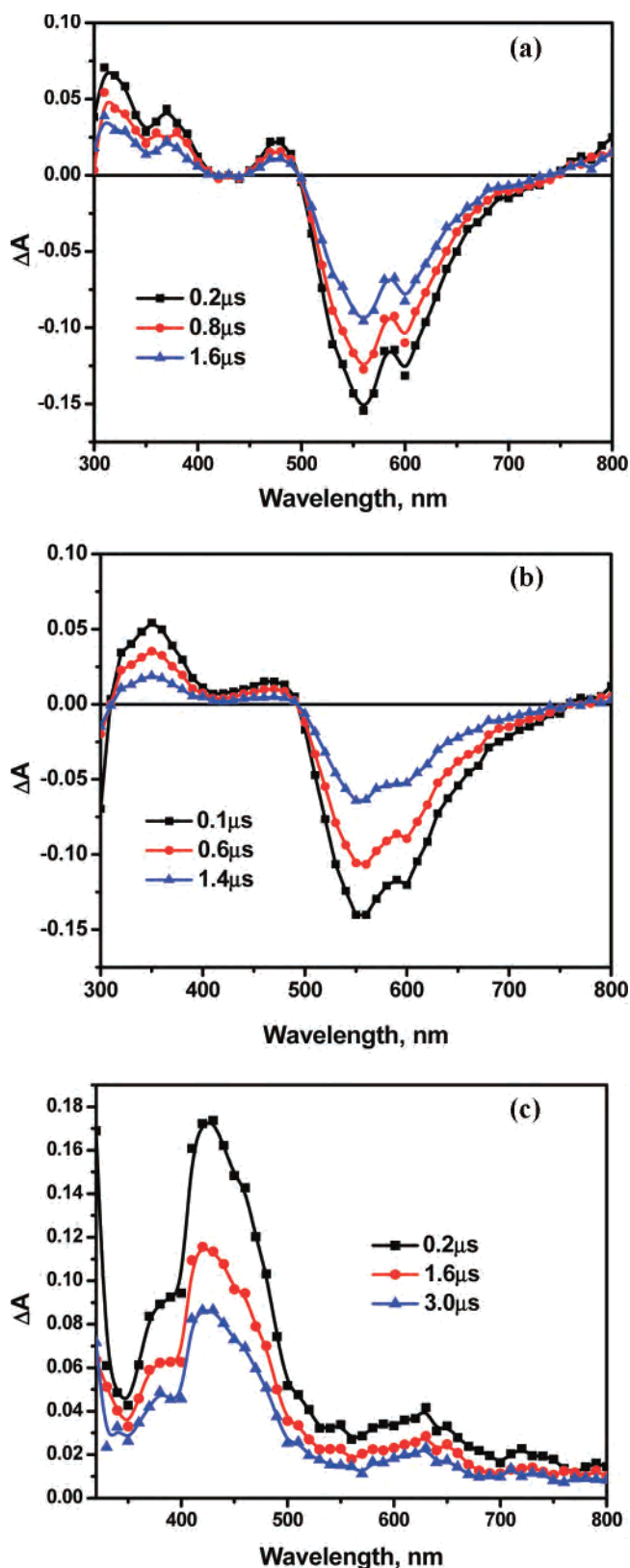
Figure 7. Nanosecond excited-state absorption spectra of **1** (a), **2** (b), and **3** (c) measured at the specified delay times in deaerated CH_2Cl_2. Spectra (a) and (b) were acquired following 430 nm excitation, whereas spectrum (c) was measured with 355 nm excitation. The apparent bleaching features in (a) and (b) are emission artifacts and are not representative of transient absorption features in this region of the spectrum.

corresponding to the peak of the ground-state absorption in **1**. The apparent bleach near 540 nm is a luminescence artifact

that cannot be corrected for in the current experimental apparatus. Therefore, long-wavelength absorption transients superimposed with the emission profile were determined using an ultrafast system, which is inherently free from long-lived, low-k_r emission artifacts. In **1**, a significant transient absorption of the relaxed excited state occurs between 550−725 nm, which maximizes near 660 nm in CH_2Cl_2 (Supporting Information). Because this feature is not consistent with the one-electron reduced dbbpy ligand, it likely represents a charge-transfer transition in the excited state such as a ligand-to-ligand or ligand-to-metal charge transfer.[10] An almost-identical long-wavelength difference spectrum is obtained for **2** (Supporting Information), measured under the same conditions, which supports the assignment for **1** provided in the previous sentence.[10] The nanosecond excited-state difference spectrum of **2** is slightly different from that of **1**, having peaks at ∼348 and ∼470 nm (part b of Figure 7). The coincidence of the excited-state difference spectra with those obtained at short wavelengths by reductive spectroelectrochemistry (Figure 6) strongly supports the conclusion that, following an appropriate laser flash, **1** and **2** produce transients most consistent with that of the dbbpy radical anion. The long-wavelength transient in **2** must be associated with a charge-transfer excited state, and given the coincidence of this data with that measured for **1**, the only conclusion from the combined nanosecond, ultrafast, and spectroelectrochemical data is that **1** and **2** possess characteristics of charge-transfer-based excited states at room temperature. The nanosecond excited-state difference spectrum of **3** following a 355 nm laser flash is shown in part c of Figure 7. This compound features a strong excited-state absorption centered at 440 with a weak shoulder at 630 nm. This transient is assigned to the ^{3}IL excited state of the metal-perturbed tda ligand because no other long-lived excited states are believed to be present in this structure. The single-exponential lifetime of this transient absorption is consistent with that determined for the phosphorescence intensity decay, which suggests they are emulating the same excited state, that of the metal-perturbed ^{3}tda ligand. Direct comparison of the spectra in Figure 7 clearly reveals distinct differences between that measured for **1** and **2** relative to **3**. Ultrafast experiments also revealed substantial differences in the relaxed excited-state spectral profiles of **1** and **2** compared with **3** (Supporting Information). The long-wavelength transient observed in **1** and **2** possesses a significantly higher cross section than the low-energy shoulder in **3**, whereas the major band in **3** is clearly much more intense than any corresponding absorption features in **1** or **2**. We conclude that there is no evidence of ^{3}tda excited-state formation in **1** at room temperature and that the ambient temperature photophysics in this structure is exclusively derived from the charge-transfer excited state. The transient spectroscopic features of the excited state in **1** are most similar to the model charge-transfer chromophore **2**.

ESR Spectroscopy. ESR spectra of the anions **1**$^-$ (Figure 8) and **2**$^-$ were obtained following in situ cobaltocene reduction of a 2:1 THF:CH_2Cl_2 sample of the appropriate neutral species. The isotropic spectrum of **1**$^-$ at 240 K ($g =$
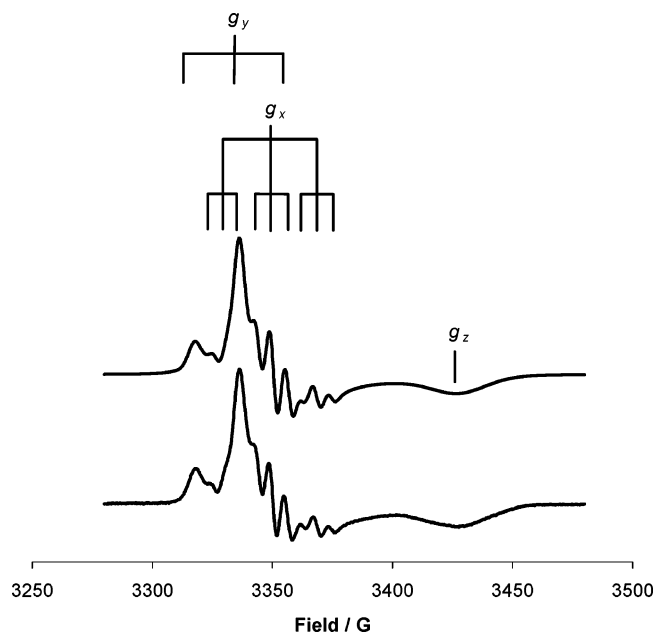
Figure 8. Simulated (top) and experimental (bottom) ESR spectra of **1**$^-$, showing the platinum hyperfine coupling seen on g_x and g_y, and (for the former) additional splitting due to the coupling to two hydrogen nuclei.

1.994) was broad and showed no discernible coupling to any nuclei, but the anisotropic spectrum obtained at 100 K was much more informative. This spectrum is rhombic (g_y = 2.013, g_x = 2.005, g_z = 1.960, $\langle g \rangle$ = 1.993), and shows coupling to the platinum nucleus (^{195}Pt, 34%, $I = {}^1/_2$) on the two low-field features ($A_y = -34 \times 10^{-4}$, $A_x = -34.5 \times 10^{-4}$ cm^{-1}).

The assignments of the x, y, and z axes and of negative values to the coupling constants follow the approach of McInnes and co-workers.[53] Using their methodology, it is possible to calculate the amount of unpaired electron density in the platinum d orbital because the difference between A_y and A_x is proportional to the amount of electron density in the metal $5d_{yz}$ orbital. Because these values are almost identical for **1**$^-$, it implies that there is essentially no $5d_{yz}$ electron density (0.1%) and that the major metal contribution to the SOMO is from the $6p_z$ orbital. This hypothesis is reinforced by the closeness of g_x and g_y; the spectrum is almost axial about z, which implies that a metallic electron is contained in a p$_z$ orbital. A similar distribution of electron density was reported for [Pt(bpy)(CN)$_2$]$^-$.[53]

A second coupling is visible on the central g_x feature, which has the effect of splitting it into a 1:2:1 triplet. In the current situation, this can only be due to coupling to two identical $I = {}^1/_2$ nuclei, which implies coupling to two hydrogen atoms either of the bipyridyl ring or of the tda ligand. From the calculated **1**$^-$ anion (as well as the calculated LUMO of **1**), there is significant electron density on the carbon atoms in the 5 positions of the pyridyl rings and none on the phenyl rings of the tda ligands, and we therefore conclude that it is spin-polarization of the protons H^5 and H$^{5'}$ that is responsible for this effect. The size of the coupling (5.5 × 10^{-4} cm^{-1}, 16.5 MHz) is very similar to that deduced by ENDOR spectroscopy for a series of Pt-

Table 5. Summary of DFT Geometry Optimizations of the Lowest Singlet and Triplet States

complex	electronic state	S$_0$ Geometry		T$_1$ Geometry
		relative energy (eV)	dipole moment (D)	relative energy (eV)
1	S$_0$ (A$_1$)	0.00	14.0	0.19
	T$_1$ (A$_1$)	1.99	1.6^a	1.79
2	S$_0$ (A)	0.00	13.5	0.21
	T$_1$ (B)	2.10	1.0^a	1.86
3	S$_0$ (A′)	0.00	9.0	0.35
	T$_1$ (A″)	2.81	10.2	2.46

^{a} The direction of the dipole moment is reversed from that in the S$_0$ state.

(4,4′-X$_2$bpy)Cl$_2$ complexes,[56] but it does not appear to have been directly observed in the ESR spectrum of this type of complex before.

Similar spectra are obtained for **2**$^-$. In the isotropic case, g_{iso} = 1.995, whereas in the anisotropic spectrum, g_y = 2.023, g_x = 2.004, and g_z = 1.962 ($\langle g \rangle$ = 1.997), with platinum coupling $A_y = -29.5 \times 10^{-4}$ and $A_x = -40.0 \times 10^{-4}$ and again with the coupling of 5.5 × 10^{-4} cm^{-1} to two hydrogen nuclei on the central (x) feature. The difference between A_y and A_x indicates that there is more d-orbital contribution to the SOMO in this case (ca. 2.25%), leading to the greater separation of g_y and g_x.

Density Functional Calculations. Geometry Optimizations. Geometry optimizations were performed on **1**−**3** in the absence of solvent, using the B3LYP functional. Table 5 summarizes the results of these calculations. Closed-shell calculations for the singlet ground states yielded structures for **1**−**3** having C_{2v}, C_2, and C_s symmetries, respectively. Frequency analyses carried out at these geometries confirmed the symmetric structures to be minima. In **1**, the tda ligand, the platinum ion, and the dbbpy ring system are coplanar, whereas in **2**, the phenyl rings are twisted 34° out of the plane that contains the dbbpy rings and the platinum ion. The calculated ground-state dipole moments range from 9 to 14 D, with the negative end of the dipole on the acetylide side of the complex. All of the subsequent TDDFT calculations were carried out at these optimized ground-state geometries.

The geometry of the lowest-energy triplet state of each complex was also optimized using an unrestricted formalism. **1** and **3** retained their ground-state symmetries of C_{2v}, and C_s, respectively, whereas **2** was found to optimize to a structure having higher symmetry, C_{2v}, than the ground state. In the T$_1$ state of **2**, the phenyl rings were found to rotate back into the molecular plane. Frequency analyses again confirmed these structures as minima. The magnitudes of the triplet-state dipole moments in **1** and **2** were found to be much smaller than in their ground states, and additionally their orientations were reversed. This is clearly indicative of the charge-transfer nature of these T$_1$ states. Also, because the two nonconjugated phenyl rings in **2** remain equivalent in the T$_1$ state, the charge-transfer transition must be delocalized over both. Further confirmation of this comes from the identical spin densities found on all of the symmetry-equivalent atoms. The dipole moment in the T$_1$

Table 6. Frontier Orbitals in S_0 from PCM (CH_2Cl_2) DFT Calculations

complex	orbital	energy (eV)	description
1	LUMO+2 (A_2)	−1.32	tda π^*
	LUMO (B_1)	−2.40	dbbpy π^*
	HOMO (B_1)	−5.22	Pt d_π − tda π
	HOMO-1 (A_2)	−5.43	Pt d_π − tda π
2	LUMO+3 (B)	−0.57	CCPh π^*
	LUMO (B)	−2.39	dbbpy π^*
	HOMO (A)	−5.30	Pt d_π − CCPh π
	HOMO-1 (B)	−5.51	Pt d_π − CCPh π
3	LUMO+1 (A′)	−1.07	Pt $6p_z$
	LUMO (A″)	−1.26	tda π^*
	HOMO (A′)	−5.25	Pt d_π − tda π
	HOMO-1 (A″)	−5.47	Pt d_π − tda π

state of **3** is similar to that in its S_0 state, indicating only minimal charge transfer. The singly occupied Kohn−Sham molecular orbitals in this triplet state correspond to π and π^* orbitals localized on the tda ligand.

Frontier Orbitals. TDDFT calculations use singly excited electron configurations formed from the ground-state Kohn−Sham orbitals to describe excited states. The ground-state orbitals contributing to the low-lying singlet and triplet states of **1**−**3** are described in Table 6 and illustrated in the Supporting Information. These were calculated using PCM formalism to model the solvent, dichloromethane. In all cases, the occupied orbitals from which electrons are promoted can be characterized as π-type orbitals delocalized over the aromatic acetylide ligand(s) combined with a Pt d_π orbital of the appropriate symmetry. The contributing unoccupied orbitals include both phenyl/tda localized π^* orbitals and, in **1** and **2**, the dbbpy π^* LUMO.

One effect arising from the enhanced π conjugation in the tda ligand is a reversed ordering of the two highest-occupied orbitals in **1** (and **3**) relative to **2**. The HOMO in **2** involves a linear combination of phenylacetylide π orbitals that is symmetric (A) with respect to rotation about the C_2 axis, whereas the HOMO-1 involves the antisymmetric combination (B). This contrasts with the ordering found in **1**, where the HOMO is antisymmetric (B_1) and the HOMO-1 is symmetric (A_2). Note that the B_1 HOMO in **1** is symmetric with respect to reflection in the plane perpendicular to the molecular plane and includes a contribution from the central acetylene bridge.

TDDFT Calculations. The typical solvatochromism of charge-transfer transitions suggests that theoretical comparisons to experiment should ideally include the effects of solvation. Therefore, TDDFT calculations of the low-lying excited states of **1**−**3** were carried out using the PCM formalism to model the dichloromethane solvent. Calculations in vacuo were also performed for reference. The results of the TDDFT calculations are summarized in Table 7. In **1** and **2**, the lowest-lying singlet and triplet states involve HOMO → LUMO excitation, and at only slightly higher energies HOMO-1 → LUMO-based S_2 and T_2 states are found. All of these transitions are of charge-transfer character, and their transition energies shift 0.6−0.7 eV higher when solvent is included. The lowest absorption bands in **1** and **2** are therefore predicted to arise from overlapped $S_1 \leftarrow S_0$ and $S_2 \leftarrow S_0$ transitions. In **1**, the $S_1 \leftarrow S_0$ transition moment lies along the C_2 symmetry axis, and the $S_2 \leftarrow S_0$ transition

moment is perpendicular to the axis. The oscillator strength for the $S_1 \leftarrow S_0$ transition in **1** is a factor of 10 larger than the $S_2 \leftarrow S_0$ oscillator strength, and thus the absorption band is dominated by a lower-energy transition polarized along the C_2 axis. Because of the inverted ordering of the highest-occupied orbitals, the description of the lowest-energy absorption band in **2** is reversed. Here the lower-energy band is weaker and polarized perpendicular to the C_2 axis.

The lowest-energy MLCT absorption band in the somewhat similar Pt(II) complex based on one bpy and two mesitylene ligands was also previously assigned to two overlapped transitions by Klein and Kaim.[63] Each overlapped transition was associated with a different set of occupied and unoccupied orbitals. The current TDDFT assignments for **1** and **2** differ in that both low-energy transitions terminate on the same lowest-energy π^* orbital of the dbbpy ligand.

A relatively low-energy T_3 state is also found in **1** that involves $\pi\pi^*$ excitation localized primarily on the tda ligand. The energy of this triplet state is fairly solvent insensitive. In a vacuum, it is calculated to lie 0.83 eV above the T_2 charge-transfer state, but in dichloromethane it is found only 0.31 eV higher. The analogous $^3\pi\pi^*$ state in **2** (not shown in Table 7) is found at a significantly higher energy because the distinct phenylacetylide ligands lack the extended conjugation of the tda ligand.

In **3**, the lowest-lying singlet and triplet states involve $\pi\pi^*$ excitation. Both are calculated to have nearly identical energies in a vacuum and in solvent. Additionally, the transition energy for the T_1 state in **3** differs by only 0.03 eV (in solvent) from the transition energy of the T_3 state in **1**. Model **3** therefore appears to provide a very good representation of the low-lying $\pi\pi^*$ excitations in **1**.

ΔSCF-Method-Shifted Transition Energies. Treating both the low-lying charge-transfer and ligand-localized $\pi\pi^*$ excited states of **1** provides a theoretical challenge. Particularly problematic is the tendency of TDDFT to significantly underestimate charge-transfer transition energies. This has been discussed previously in some detail.[57−60] One proposal to treat such states is based on a hybrid approach, which uses DFT transition energies derived from the ΔSCF method as a reference point for shifting transition energies derived from another method.[57,58] ΔSCF-method transition energies are obtained by subtracting the ground-state DFT energy from the energy of an excited state calculated as an open-shell configuration using an unrestricted DFT formalism. Charge-transfer transition energies calculated from the ΔSCF method tend not to suffer from the same systematic underestimation, as when TDDFT is used to calculate them directly. The use of the ΔSCF-method transition energies to shift the distance dependent configuration interaction singles transition energies of the low-lying charge-transfer transitions in a linked zincbacteriochlorin-bacteriochlorin was extensively demonstrated by Dreuw and Head-Gordon.[61] Whereas TDFFT calculations yielded several charge-transfer transitions below the $\pi\pi^*$ Q bands, application of the ΔSCF

(63) Klein, A.; Kaim, W. *Organometallics* **1995**, *14*, 1176−1186.

Table 7. Summary of PCM TDDFT Calculations

complex	electronic state	main configuration	Vertical Transition Energy (eV)			oscillator strength
			vacuum	CH_2Cl_2	shifted[a]	
1	$T_1(A_1)$ MMLCT	HOMO → LUMO	1.50	2.18	2.68	
	$T_2(B_2)$ MMLCT	HOMO-1 → LUMO	1.68	2.31	2.81	
	$S_1(A_1)$ MMLCT	HOMO → LUMO	1.75	2.37	2.87	0.234
	$S_2(B_2)$ MMLCT	HOMO-1 → LUMO	1.80	2.47	2.95	0.021
	$T_3(B_2)$ $\pi\pi^*$	HOMO → LUMO+2	2.43	2.49	2.87	
2	$T_1(B)$ MMLCT	HOMO → LUMO	1.61	2.25	2.74	
	$T_2(A)$ MMLCT	HOMO-1 → LUMO	1.80	2.41	2.90	
	$S_1(B)$ MMLCT	HOMO → LUMO	1.71	2.35	2.84	0.028
	$S_2(A)$ MMLCT	HOMO-1 → LUMO	2.05	2.62	3.11	0.134
3	$T_1(A'')$ $\pi\pi^*$	HOMO → LUMO	2.43	2.46	2.84	
	$S_1(A'')$ $\pi\pi^*$	HOMO → LUMO	3.34	3.39	3.77	0.098

[a] Shifts derived from the comparison of TDDFT and ΔSCF-method transition energies are applied to the CH_2Cl_2 vertical transition energies. See text for the values of the shifts applied to the charge-transfer and ligand-localized $\pi\pi^*$ transitions in each complex.

Table 8. Calculated Absorption and Emission Properties

complex	Absorption Wavelength[a] (nm)		Emission Wavelength[a] (nm)	
	vertical $S_2 \leftarrow S_0$[b]	vertical $S_1 \leftarrow S_0$	vertical $T_1 \rightarrow S_0$	0−0 $T_1 \rightarrow S_0$
1	418 (427)	432 (427)	541 (562)	501
2	399 (397)	436 (397)	542 (560)	497
3		329 (355)	581	497 (497)

[a] Experimental values given in parentheses. [b] The absorption maximum for the longest wavelength absorption band in Pt(dbbpy)(tda) and Pt(dbbpy)-(CCPh)$_2$ is predicted to arise from overlapped $S_2 \leftarrow S_0$ and $S_1 \leftarrow S_0$ charge-transfer transitions.

method correction moved all of the charge-transfer states to energies above the Q states, in agreement with experiment.

Here, we investigate a similar approach using ΔSCF-method-derived transition energies for the lowest triplet state of **1** and **2** (Table 5) to shift the charge-transfer transition energies derived from TDDFT calculations. Comparison of Tables 5 and 7 shows that the vertical transition in a vacuum to T_1 in **1** is calculated to be 0.49 eV higher by the ΔSCF method. Therefore, in Table 7, a column is included, which applies this same 0.49 eV shift to the TDDFT charge-transfer excitation energies calculated for **1** in dichloromethane. An identical shift was derived in the same way for charge-transfer excitations in **2**.

Characterization of the Absorption and Emission Features. To further investigate the validity of applying the ΔSCF-method-derived shift to the TDDFT charge-transfer transition energies comparisons can be made to the experimental absorption and emission spectra (Table 8). The low-energy absorption bands in **1** and **2** are calculated to arise from overlapped $S_1 \leftarrow S_0$ and $S_2 \leftarrow S_0$ transitions. After shifting, the band in **1** is predicted to arise from a strong transition at 2.87 eV or 432 nm and a weaker transition at 418 nm. The experimental absorption maximum is observed at 427 nm in dichloromethane (Table 3). Similarly, the low-energy absorption band in **2** is predicted to be derived from a weak 436 nm transition and a stronger 399 nm transition. The experimental band maximum is seen at 397 nm.

Emission data can be used to check the calculated triplet-charge-transfer transition energies, although geometrical relaxation in the emitting T_1 state should be taken into account. The geometry optimization calculations summarized in Table 5 suggest that the T_1 states in **1** and **2** drop in energy

by 0.20 and 0.24 eV, respectively, following relaxation from their Franck−Condon geometries. In their relaxed T_1 geometries, the ground-state energies of **1** and **2** rise by 0.19 and 0.21 eV. Thus, the calculated vertical $T_1 \rightarrow S_0$ transition energies in Table 7 need to be reduced by the sum of these two contributions to compare with experiment. With these effects included, the vertical emission in **1** and **2** is predicted to occur at 541 and 542 nm, respectively. These values compare with the observed 562 and 560 nm band maxima.

Although these comparisons give strong support for the ΔSCF-method-derived shifts to correctly locate charge-transfer transition energies, **3** contains a lowest-lying $^3\pi\pi^*$ state, and **1** must contain a similar ligand-localized triplet state. The vibronically resolved emission from **3** shows a strong 0−0 transition at 497 nm. The energy for this 0−0 transition by PCM TDDFT is calculated to be 2.11 eV or 588 nm after taking into account geometrical relaxation in the T_1 state. However, if the ΔSCF-method energy, Table 5, is compared to the TDDFT energy, Table 7, the $^3\pi\pi^*$ TDDFT energy is found to be 0.38 eV lower. This suggests that the PCM TDDFT energies for the $^3\pi\pi^*$ state in **3** should be shifted by 0.38 eV. Although ΔSCF-method-derived shifts were previously applied only to the charge-transfer transition energies, when the shift is applied to the T_1 state in **3**, a 0−0 transition at 497 nm is predicted.

The origin of the fortuitous agreement between experiment and theory in **3** is not clear. However, it is obvious that shifting the energies of the triplet charge-transfer states in **1** and not shifting the energy of the $^3\pi\pi^*$ state, T_3, leads to the incorrect prediction that the $^3\pi\pi^*$ state is at lower energy and therefore is the emissive triplet state. The broad, unstructured profile of the emission band in **1** is inconsistent with a lowest-lying $^3\pi\pi^*$ state. If the same 0.38 eV shift derived for **3** is applied to **1**, the vertical energy of the $^3\pi\pi^*$ state becomes 2.87 eV. This value is 0.19 and 0.06 eV above the two lower-energy charge-transfer triplet states. With a predicted separation of only 0.19 eV in dichloromethane, it is not surprising that the charge-transfer and $\pi\pi^*$ triplet states might reorder in a more polar solvent, such as seen experimentally in the low-temperature EtOH/MeOH glass.

Conclusions

In summary, **1**, representing a new class of Pt^{II} charge-transfer chromophores bearing a cyclic diacetylide ligand has

been prepared, photophysically characterized, and directly compared to the model chromophores **2** and **3**. The crystal structure of **1** displays approximate C_{2v} symmetry in the solid state. The static and time-resolved absorption/emission properties of **1** and **2** at room temperature in fluid solution are consistent with an excited state of predominately charge-transfer character. This assignment is congruent with a body of spectroscopic evidence, including definitive reductive spectroelectrochemical measurements. The metallacyclyne structural motif yields a highly luminescent rigid molecule that exhibits reduced nonradiative decay and a much longer excited-state lifetime relative to that for model chromophore **2** even though the structures exhibit nearly identical emission spectra at room temperature. Side-by-side comparison of the absorption/emission data of **1** and **2** with that of **3** definitively rules out any contributions of a tda-localized triplet state to the photophysics at room temperature. In low-temperature glasses, the situation is somewhat more complex, as the emission spectra of **1** and **3** become nearly co-incident in energy and band shape, indicating an inversion of excited states in **1** between room temperature and 77 K. The luminescence intensity decay of **1** in both MTHF and 4:1 EtOH:MeOH at 77 K exhibits complex kinetics, being adequately fit using a biexponential model. Time-resolved emission spectra reveal band narrowing and a concomitant small blue shift with time at 77 K, which supports the presence of two identifiable emitting states under these conditions. The short and long lifetime components are both longer-lived relative to the charge-transfer model system **2** and are both shorter-lived than the pure ^{3}IL phosphorescence observed in **3** at low temperature. We speculate that this result indicates strong, but incomplete, triplet-state mixing between the charge-transfer and tda ligand-localized excited states at 77 K. PCM TDDFT calculations performed on **1**−**3**

in a CH_2Cl_2 continuum revealed the molecular orbitals, dipole moments, energies, and oscillator strengths for the various electronic transitions in these molecules. Application of the ΔSCF-derived shift method to the calculated transition energies in the CH_2Cl_2 solvent continuum yielded good agreement between theory and experiment for each molecule in this study and suggests the broader application of this treatment to charge-transfer chromophores in condensed phases. On the basis of the data presented in this contribution, we recommend that the low-energy optical transitions in **1** and **2** be termed mixed-metal ligand-to-ligand charge transfer (MMLL′CT),[27,55] to highlight the intimate electronic coupling observed between the metal d orbitals and acetylide π orbitals in these and related structures. Current work has extended the use of the tda ligand, which has already yielded new Pt(II) structures with strong ground-state charge-transfer absorptions in the red.[64]

Supporting Information Available: DFT-calculated molecular orbitals, time-resolved photoluminescence data, additional nanosecond TA data, ultrafast TA difference spectra, and the CIF of **1**. This material is available free of charge via the Internet at http://pubs.acs.org.

IC701103U

---

(64) Collaborative work in progress.